J Mater Sci (2017) 52:415–430

A 3D micromechanical study of hygroscopic coiling deformation in *Pelargonium* seed: from material and mechanics perspective

Che Zhao[1], Qingping Liu[1,*], Luquan Ren[1], Zhengyi Song[1], and Jingchun Wang[1]

[1] *Key Laboratory of Bionic Engineering (Ministry of Education, China), Jilin University, P.O. Box 130022, Changchun, People's Republic of China*

Received: 22 June 2016
Accepted: 24 August 2016
Published online: 7 September 2016

ABSTRACT

The awned seeds of the family *Geraniaceae* are special seed-dispersal units. The awns can generate periodic coiling and uncoiling movement through interaction with the diurnal humidity cycle. To investigate how this natural actuator acquires the remarkable property, we determined the three-dimensional morphological features of the coiling awns of *Pelargonium peltatum* through X-ray microtomography (micro-CT). Many streaks with sharp corners were found distributed in the surface of the inner layer cells, indicating there are two different microfibril angles (MFAs) in the special tilted helix structure of each one cellulose fiber within the cell wall. A simplified mechanical model of the cell wall was developed. Moreover, finite element method was conducted based on the proposed model to analyze the basic mechanism of the coiling deformation. The results showed that stiff cellulose fibers with special tilted helix structures could direct the shrinkage forces resulted from the matrix, so as to generate torsional and bending movement simultaneously. Therefore, the inner layer cell could generate an anti-clockwise coiling deformation macroscopically. In addition, effects of other structural factors including fiber frequency of the cellulose fiber skeletons, modulus ratios between the fibers and matrix, and macroscopical combination among the cells on the degree of the coiling deformation were also studied. The results determined in this work may benefit the development of new kind of intelligent composites.

Introduction

Living creatures suffer from various stimuli such as sound, light, electricity, heat, and gravity. Of these, passive actuation is a unique natural system in seed-dispersal units of some plants [1]. Tissues attached to these units undergo senescence and eventually die after being separated from their mother plant. However, these units can still direct their hygroscopically active accessories to propel ripe seeds into the soil or

Address correspondence to E-mail: liuqp@jlu.edu.cn

DOI 10.1007/s10853-016-0341-6

release them in a suitable space by interacting with environmental changes in humidity. This passive actuation mechanism has evolved in various plants, such as pine cones [2, 3], moisture sensitive spore capsules of some kinds of mosses [4], desert plant *Anastatica hierochuntica* [5], seed pods of *Bauhinia variegate* [6], wild wheat awns [7, 8] and awned seeds of family *Geraniaceae* [9–14].

Passive hygroscopic movements rely on reversible anisotropic swelling or shrinkage deformation of plant tissues controlled by the complex architecture of the cell wall. These plant tissues typically consist of fiber cells whose cell wall consists of cellulose macrofibrils (formed from bundles of cellulose microfibrils approximately 10–20 nm in diameter, and aligned parallel to one another) with a preferred orientation [15, 16]. Macrofibrils are embedded in a highly swellable matrix, which consists of amorphous materials, such as hemicelluloses, lignin, pectin, and structural proteins [17–19]. This cell wall assembly can be considered a natural fiber reinforced composite because of significant differences in stiffness between the reinforcement fibers (cellulose microfibrils) and the matrix material [20, 21]. The angle between cellulose microfibrils and the cell axis (MFA) is a critical parameter that can passively change tissue geometry [22]. The intermolecular hydrogen bonding between the network structures of the swellable matrix can reversibly combine with water molecules. Consequently, the hemicelluloses and other swellable matrix materials between the cellulose macrofibrils has the property of swelling (or shrinkage) reversibly. Therefore, deformation of the cell wall becomes extremely anisotropic, and occurs in the direction perpendicular to the fibril orientation more easily [23].

Many studies have shown that most dead hygroscopic tissues primarily consist of two basic fibrous layers with different MFA; hence, hydration-mediated expansion/shrinkage characteristics vary when wetted or dried. Two attached layers that swell or shrink in different directions can induce different passive movements of plant organs because the deformation of one layer is restricted by another. Through this complicated mechanism, biological actuators can generate various deformations, such as bending, rolling, twisting, and torsion [24–26]. However, in the family *Geraniaceae*, the coiling motion of their awns requires only one homogenous inner layer, which consists of a cluster of inherently coiling cells. Cellulose microfibrils embedded in their cell walls are arranged in a tilted helix [11]. In contrast to a normal helix, where MFA keeps constant for any azimuthal direction, MFA in the tilted helix arrangement changes with the azimuthal direction, with different signs at opposite sides of the cell wall [13]. Furthermore, this type of coiling cells is manifested by the awns of all genera in the *Geraniaceae* family [12]. Our long-term goal is to develop a biomimetic fibrous actuator inspired from the hygroscopic coiling awns of *Geraniaceae*. This new actuator with small size and light weight can generate coiling deformation spontaneously and no additional energy source and electronic control system are required. Up to date, numerous studies are mainly based on 2D cross-section investigation of hygroscopic tissues through scanning electron microscopy, small-angle X-ray scattering (SAXS), or polarized light microscopy to infer the entire configuration of hygroscopic coiling awns. As such, the effects of structural complexity of coiling awns, especially the specific configuration of the fiber skeleton within one cell and mechanism of the connection among cells have not been paid more attention.

X-ray microtomography (micro-CT) is a valuable tool used to repeatedly and nondestructively measure the three-dimensional (3D) characteristics of biological tissues at the same sites with a micrometer-level precision. This tool has been widely employed to study plant anatomy at the tissue or cellular level [27, 28]. Besides, in this study, we highlight *Pelargonium* (Fig. 1), a representative genus of the *Geraniaceae* family. The coiling awn of seeds from this plant is very thin and delicate and is, therefore, suitable for micro-CT measurement (to produce high-resolution results). Moreover, the inner layer consists of only one row of parallel arranged cells. This kind of arrangement is simpler than that of *Erodium*. Thus, 3D microstructure of the hygroscopic coiling awn of *Pelargonium peltatum* was examined through micro-CT to find the structural factors which may influence the deformation. Finally, the basic mechanism of the coiling behavior was analyzed using a simplified mechanical model and Finite Element (FE) method. The results determined in this work elucidate the mechanism of passive actuation of hygroscopic coiling further and could benefit the development of new kind of intelligent composites.

Fig. 1 Representative frames showing the recoiling process of *Pelargonium peltatum* awned seed dried at room temperature from the initially wet condition (*scale bar* 5 mm).

Materials and methods

X-ray microtomography scanning

Fresh awned seeds of *P. peltatum* were obtained from local commercial sources. Dry and saturated awn specimens from the same seed were scanned by SkyScan 1172 high-resolution micro-CT scanner (Skyscan, Bruker, Belgium) at room temperature. The saturated specimen was enclosed in a hermetically sealed clear plastic tube. Distilled water (15–20 ml) was added to the tube to maintain the saturated state. After scanning, 2525 section images of the dry (pixel size of 0.67501 μm) and saturated (pixel size of 0.74315 μm) specimens were reconstructed in SkyScan software (SkyScan NRecon 1.6.9.4). For the dry specimen, reconstruction parameters including ring artifact correction, beam hardening artifact correction, and smoothing level, were defined as 6, 34, and 1 %, respectively, as well as 7, 3, and 0 %, respectively, for the saturated specimen. After the reconstruction, the high-quality images were imported into SkyScan DataViewer 1.5.0 software to generate three section views, namely, coronal (x–z plane), sagittal (y–z plane), and transaxial (x–y plane) (Fig. 2). More than 50 consecutive orthographic views of the saturated awn specimen were captured to determine geometric parameters. Length, cross-section width, and wall thickness of cells in the inner layer of the awn tissue were measured by image analysis software SkyScan CTAn1.13.5.1.

A total of 500 consecutive slice images from one part of the specimen were captured and reconstructed as a volume element. Volume variations in each of the three volume elements were measured by SkyScan CTAn, and the average value was determined. Thus, the average volume strain of the awn tissue (ΔV) was obtained:

$$\Delta V = \frac{V_0 - V}{V} \times 100(\%), \tag{1}$$

where V and V_0 are the volume of the specimen with saturated and dry state, respectively.

Finite element analysis

S2 layer (the thickest and mechanically dominating layer of the whole cell wall [22]) in the inner layer of the coiling awn was idealized as a thin-walled hollow fiber reinforced rectangular tube (Fig. 3). The geometry parameters of the rectangular tube including height, width, and wall thickness were assumed to be H, W, and t, respectively. The model was then imported into Abaqus (V12-1, Simulia, USA) for finite element simulation. Cellulose macrofibrils embedded in the S2 layer were defined as linear beams with circular profiles (radius of r) and composed of B31 elements (2 node linear beam in space). Young's modulus (E_f) and Poisson's ratio (v_f) of these beams were set to 135000 (MPa) and 0.1, respectively. These values are comparable with plant cells used in previous studies [29–32]. One beam is arranged in a special tilted helix. Consequently, there are two different MFAs θ_1 and θ_2 in the opposite sides of the helix (Fig. 3a). Assemble of the beams with same structures constitute the complete fiber skeleton of the FE model and denoting I as the interval between two adjacent beams (Fig. 3). Here, a dimensionless parameter F ($F = 2r/I$) was employed to indicate the frequency of the fiber skeleton.

From the morphology features exported by SkyScan CTAn, we found that the span S ($S = t/W$) was

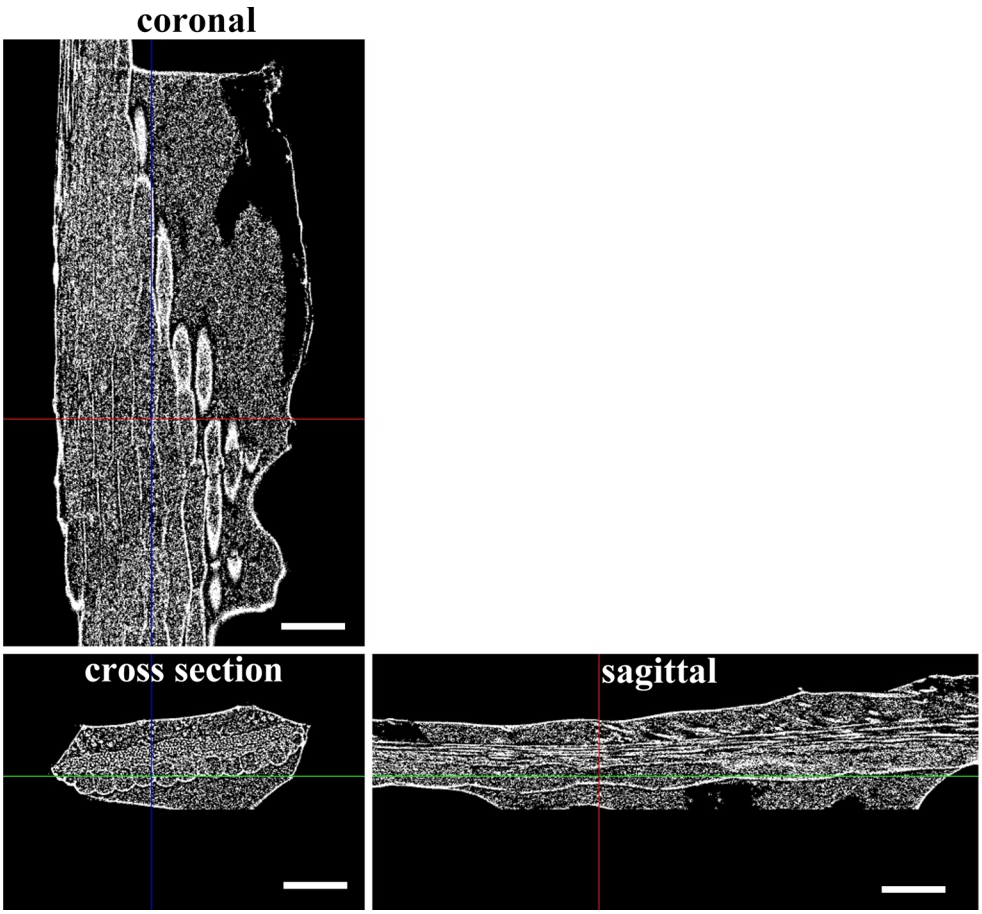

Fig. 2 Three section views of the awn specimen under saturated condition generated by the SkyScan DataViewer (*scale bars* 200 μm).

much less than 1/10. Thus, the matrix material of the cell wall was simplified as a continuum shell (homogeneous) which composed of S4R elements (4 node doubly curved thick shell with finite membrane strains, reduced integration) and the accuracy of the mesh was ascertained (Fig. 3b). The components of

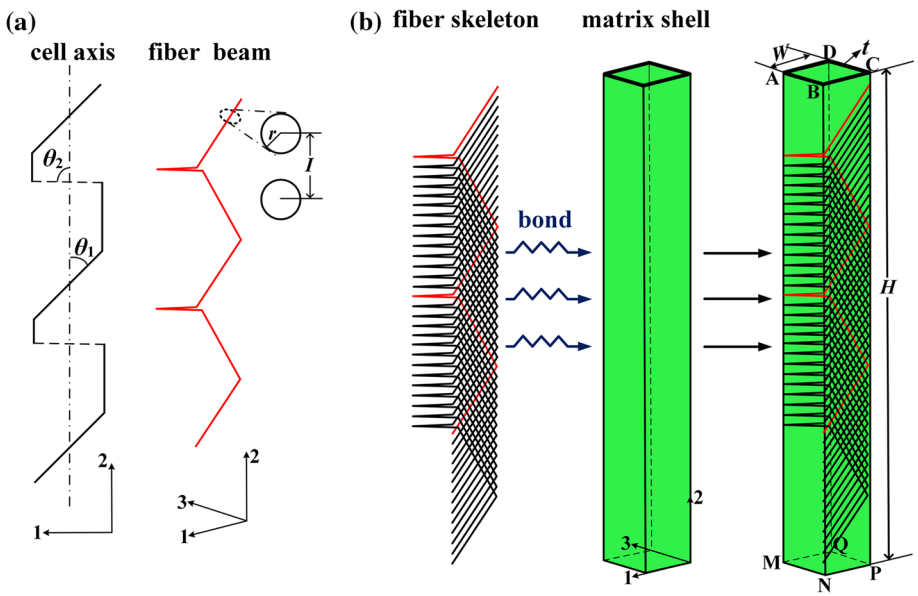

Fig. 3 Diagram illustrated the microstructure of the FE cell wall model (*axes* represent the local coordinate systems). **a** Cellulose fiber was modeled as a linear beams with radius of r and in a tilted helix arrangement, θ_1 and θ_2 indicate two different MFAs of the helix, I indicate the interval between two adjacent beams. **b** An entire cell wall was modeled as the fiber skeleton embedded in the matrix shell with height of H and width of W.

the matrix material are quite complicated and the property may change during extraction from the plant due to technical limitations. Combined the data obtained from Cousins and Salmén [33–36] and the recent work about the mechanical properties of plant cell walls soft material at the subcellular scale [37], we considered those components as a homogenous material and its Young's modulus (E_m) and Poisson's ratio (v_m) were assumed to be 600 and 0.25 MPa, respectively. Meanwhile, it was assumed ideal bonding existed at the fiber-matrix interfaces and no strain discontinuity occurred between them. Furthermore, the sequentially coupled thermal-stress analysis module of Abaqus was employed to simulate the isotropic shrinkage of the compliant matrix. The expansion coefficient was set as η ($\eta = \Delta V/3$). The 3D analysis results exported by SkyScan CTAn reveal that the volume strain (3η) of the awn specimen is 24 ± 3.52 % ($\eta = 0.08$). Then, the slow recoiling process of the simplified model was segmented into five analysis steps in Abaqus standard solver. The initial temperature field of the model was predefined as 1 °C, which will reduce 0.2 °C at each step during the whole analytical process. For boundary conditions, the bottom surface of the tube model (MNPQ) was pinned and no constraints were defined for the remaining surfaces.

Results

Three-dimensional morphology features of the awn tissue

In the study, the top part of the active saturated awn tissues is examined using 3D images reconstructed from SkyScan NRecon (Fig. 4). The cross-section images show two homogeneous layers, which exhibit different cell wall morphologies and are connected by a layer of middle lamella tissue (Fig. 4c). The inner layer (facing inward to the coil) consists of a row of parallel cells with relatively large profile dimension. Shapes of the ventral and dorsal sides of the cell walls are arc and those of their anterior and posterior sides are flat. The width and wall thickness of these cells are 71.27 ± 9.11 and 5.72 ± 1.26 μm, respectively. The lateral sides of two adjacent cells are bound by thin middle lamella layer. One column of cells aligned with the longitudinal direction of this part consists of four or five cells (300–600 μm in height), as shown in Fig. 4d. The joint part between two end-to-end cells exists an obvious malposition, come into being an abnormal middle lamella region (indicated by the arrows).The outer layer (facing outward from the coil) consists of four layers of regular arranged cells with large ratio of length-to-diameter (Fig. 4e). The configuration of this layer is similar to that of the laminated composite material.

Figure 5 shows the 3D images of the dry awn. A column of cells hinged with one another, similar to a head and tail-connected string shaped link, cooperates to produce a macroscopic coil. Moreover, the structure of the middle lamella tissues, which connect two cells with side-to-side arrangement, is not compact and possesses many small cavities (indicated by the arrows in Fig. 5c). Numerous streaks aligned along the cell axis can be observed on the surface of the coiling cells (inner layer) because crystalline cellulose fibers could be irradiated by X-ray (Fig. 5d). Morphology of each streak shows the change in its orientation. This feature supports the assumption that cellulose fibers are arranged in a tilted helix [11–13] from a 3D perspective. Thus, we propose that the complete skeleton within the inner layer cell wall consists of numerous cellulose fibers with tilted helix arrangement and these fibers are aligned along the cell axis with small intervals (shown in Fig. 3b).

Simplified mechanical model of the inner layer cell wall

To verify the proposed structure, a simplified mechanical model is built. A small cuboid with h in height and W in width is extracted from the cell wall model randomly. As shown in Fig. 6a, a rectangular sheet with 4 W in width is obtained after virtually cutting the cuboid along a vertical line. Diagonal of this rectangular sheet represents the longest cellulose fiber within the cuboid. According to the mechanical property that listed in "Finite Element Analysis" section, the cellulose fibers with huge stiffness could be considered as inextensible compared to the soft matrix. Consequently, shrinkage of the matrix in the fiber direction was restricted and strain of the whole sheet (ε_θ) will occur preferentially in the direction that is normal to stiff fibers.

If keeping lengths of the stiff fibers as constant, distance between the fibers will change from u_0 to u' under the effect of ε_θ and shape of the sheet deforms from rectangular into rhomboid. The angle between

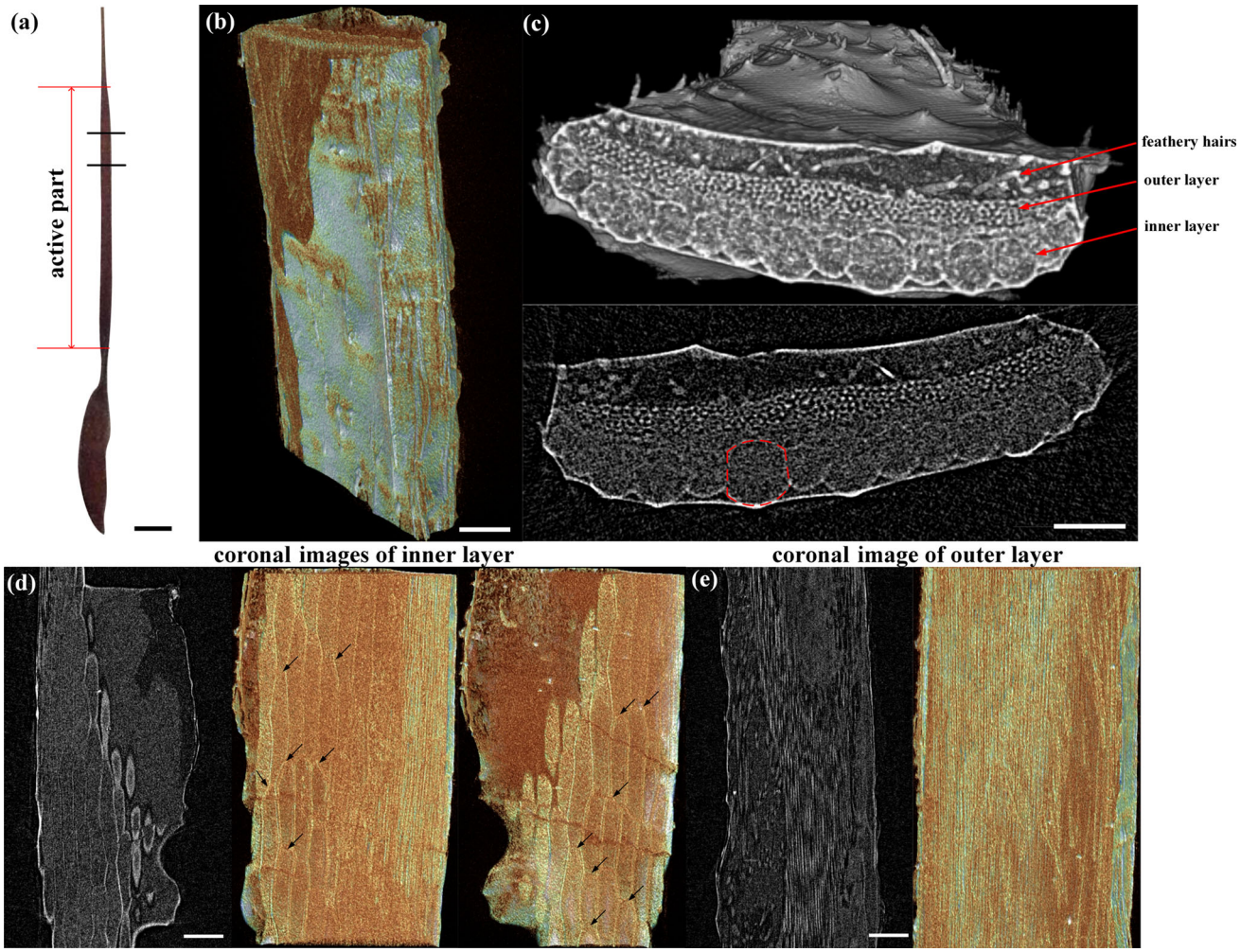

Fig. 4 **a** Macroscopic morphology of the saturated awned seed of *P. peltatum*. **b** 3D morphology image of the top part of the saturated active awn tissue. **c** Micromorphology images of the awn cross-section at the active region. **d** Coronal section images of the inner layer of the saturated awn tissue. *Arrows* indicate the joint interface between two articulated cells. **e** Coronal section images of outer layer of the saturated awn tissue. *Scale bars* **a** 2 mm, **b** 200 μm, **c** 100 μm, and **d**, **e** 200 μm.

the horizontal edges of rectangle and rhomboid (ω_1) can be calculated according to the geometrical relationship shown in Fig. 6a:

$$\omega_1 = \theta - \arctan[(1-\varepsilon_\theta)\tan(\theta)] \tag{2}$$

Applying a similar calculation for the angle between two vertical edges (ω_2):

$$\omega_2 = \frac{\pi}{2} - \theta - \arctan[(1-\varepsilon_\theta)\cot(\theta)]. \tag{3}$$

If the bottom line of the rhomboid remains in the same plane as the original rectangle, the whole sheet will turn by a total angle of $\omega_1 + \omega_2$ and has a smaller height of h'. Eventually, shape of the new cuboid constructed by four rhomboid segments will deform into twisting (Fig. 6b). This phenomenon indicates that helix structure of the stiff cellulose fibers can direct the shrinkage forces generated by matrix, so as to form a torque (T). Shear strain produced by this torque ($\tan\gamma$) can be calculated by combining Eqs. (2) and (3):

$$\begin{aligned}\tan\gamma &= \tan(\omega_1+\omega_2)\\ &= \tan\Big(\frac{\pi}{2} - \arctan[(1-\varepsilon_\theta)\tan\theta]\\ &\quad - \arctan[(1-\varepsilon_\theta)\cot\theta]\Big)\end{aligned} \tag{4}$$

Furthermore, the axial strain (ε_h) (parallel to the cell axis) of the cuboid can be calculated by geometrical relationship:

$$\varepsilon_h = \frac{h'-h}{h} = \frac{\sin\varphi}{\cos\theta} - 1 = \frac{\sin[\arctan((1-\varepsilon_\theta)\cot\theta)]}{\cos\theta} - 1. \tag{5}$$

Examples of $\tan\gamma$ changing with the MFA (θ) for three different ε_θ are shown in Fig. 7a. Under the

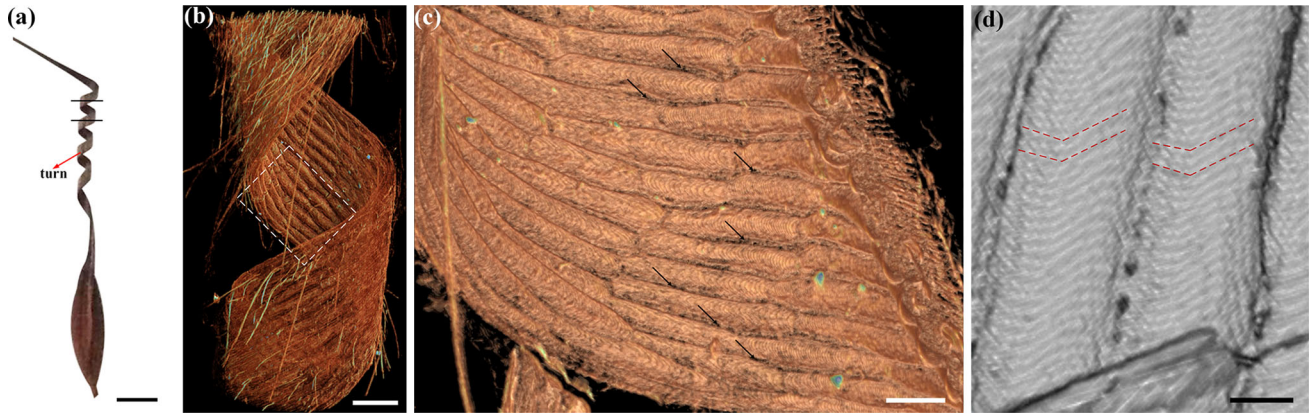

Fig. 5 **a** Macroscopic morphology image of the dry awned seed of *P. peltatum*. **b** 3D morphology image of the top part of the dry active awn tissue. **c**, **d** Enlarged views of the surface morphology of the inner layer cells. *Arrows* indicate the small cavities in the structure of the middle lamella tissues. *Dash lines* indicate change in the orientation of one streak. *Scale bars* **a** 2 mm, **b** 200 μm, **c** 100, and **d** 30 μm.

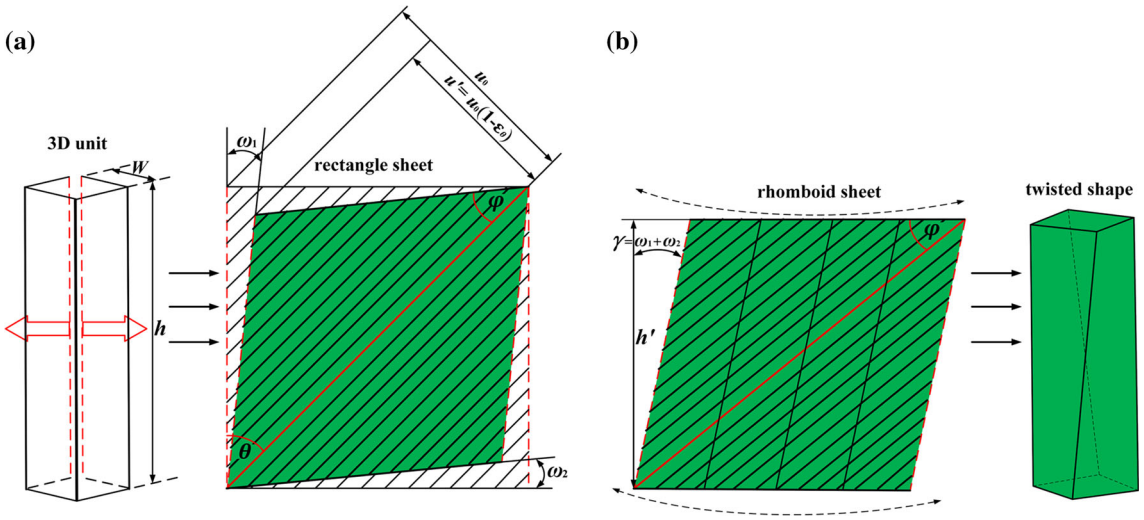

Fig. 6 Deformation of the cell wall model during shrinkage with helix cellulose fibers (example with $\theta = 45^{\circ}$). **a** A small cuboid extracted from the cell wall virtually cut open along a *vertical line* and deforms from the *rectangular sheet* into a rhomboid according to the shrinkage process (distance between the stiff fibers decreased from u_0 to u'), ω_1 indicates angle between the *horizontal edges* of rectangle and rhomboid, ω_2 indicates angle between two *vertical edges* of them. **b** Shape of the new cuboid constructed by four rhomboid segments deformed into twisting according to the assumption that the *bottom line* of the rhomboid remains in the same plane, h' indicates height of the twisting cuboid, and $\varphi = \frac{\pi}{2} - \theta - \omega_2$.

same MFA, torsion becomes more pronounced with the increasing of ε_θ. In the range of $0^{\circ} < \theta < 90^{\circ}$, the graph belongs to a symmetric periodic function and magnitudes of $\tan\gamma$ reach the maximum at $\theta = 45^{\circ}$. As shown in Fig. 7b, the axial strain (ε_h) are always shrinkage, the magnitudes ($|\varepsilon_h|$) of which monotonically increasing with θ and will reach the maximum when θ takes 90°. Thus, within the range of $45^{\circ} < \theta < 90^{\circ}$, magnitudes of the $\tan\gamma$ and ε_h have two different varying patterns. Fibril orientations in awn of representative species from family *Geraniaceae* had been examined by small angle X-ray scattering (SAXS) [12]. In *P. peltatum* awn, 2D SAXS pattern obtained from its inner layer displays a single streak that is off the meridian. This phenomenon indicated that there is a tilt angle (θ_t) between the cellulose helix axis (black line in Fig. 7c) and the cell axis (red line in Fig. 7c). The measurement results of θ_t and the

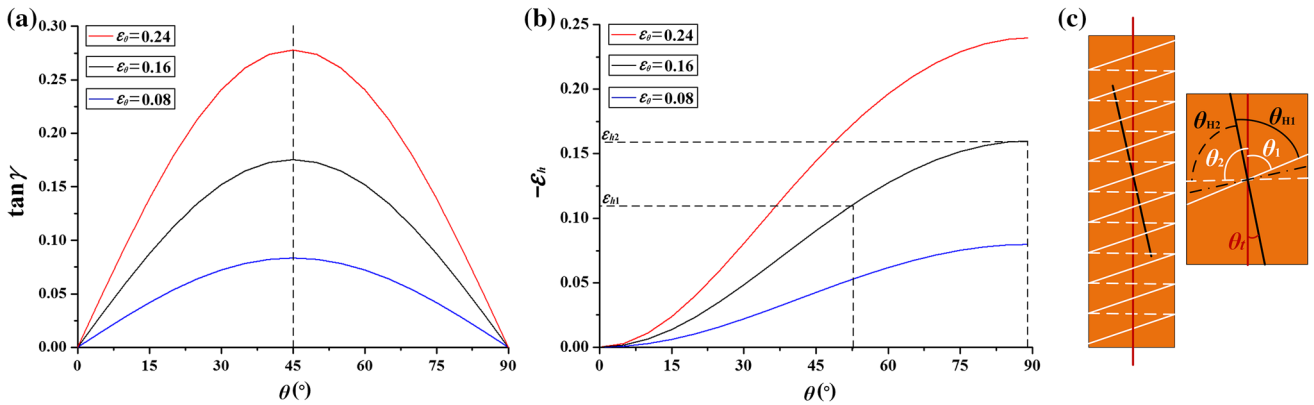

Fig. 7 **a** Interdependency of MFA (θ), shrinkage strain normal to the fibers ε_θ and shear strain (tan γ) according to the shrinkage process. **b** Interdependency of θ, ε_θ, and axial strain (ε_h) according to the matrix shrinkage, ε_{h1} and ε_{h2} indicate the axial strains of shells with different MFAs. **c** Schematic illustrates the tilted helix organization of one cellulose fiber which was redrawn according to the 2D SAXS pattern [12]. θ_1 and θ_2 indicate the different MFAs in opposite of the tilted helix, respectively. θ_t indicates the tilt angle between the cellulose helix axis (*black line*) and the cell axis (*red line*). θ_H indicates the MFA in relation to the cellulose helix axis.

MFA in relation to the cellulose helix axis (θ_H) are 19° and 70°, respectively. Moreover, based on the symmetry of helix ($\theta_{H1} = \theta_{H2}$), the magnitudes of two different MFAs θ_1 and θ_2 can be calculated: $\theta_1 = \theta_H - \theta_t = 51°$, $\theta_2 = \theta_H + \theta_t = 89°$. The results are just close to the extreme values of function (4) and (5). The feature of $\theta_1 = 45°$ can ensure the matrix generate enough torque and incompatible elasticity of the shells with relative lower and higher MFAs ($\theta_1 = 45°$, $\theta_2 = 90°$) in opposite sides of the cell wall will induce the whole cuboid to bend with a moment (M_n). Under the combined effect of T and M_n, the cell wall model generates an anti-clockwise coiling deformation macroscopically (Fig. 8b). Then the geometric model shown in Fig. 3b is imported into Abaqus for FE analysis. Fourteen tube models with different magnitudes of θ_1, θ_2 and θ_t are built for comparison (Table 1) and their structural parameters which are listed in Table 2 remain unchanged. The simulation results show that configuration of the deformed tubes are curves in 3D space (Fig. 9a). For $\theta_t = 0$ ($\theta_1 = \theta_2$), the curves are purely twist and the most turns exist in the case of $\theta_1 = \theta_2 = 45°$. This is in agreement with the calculation of function (4). For $\theta_t > 0$, the curves convert from twist to the anti-clockwise coil gradually and pitch angle of the coil decreases with the increase of θ_t. However, configuration of the curves depend not only on the tilt angle. Even values of θ_t

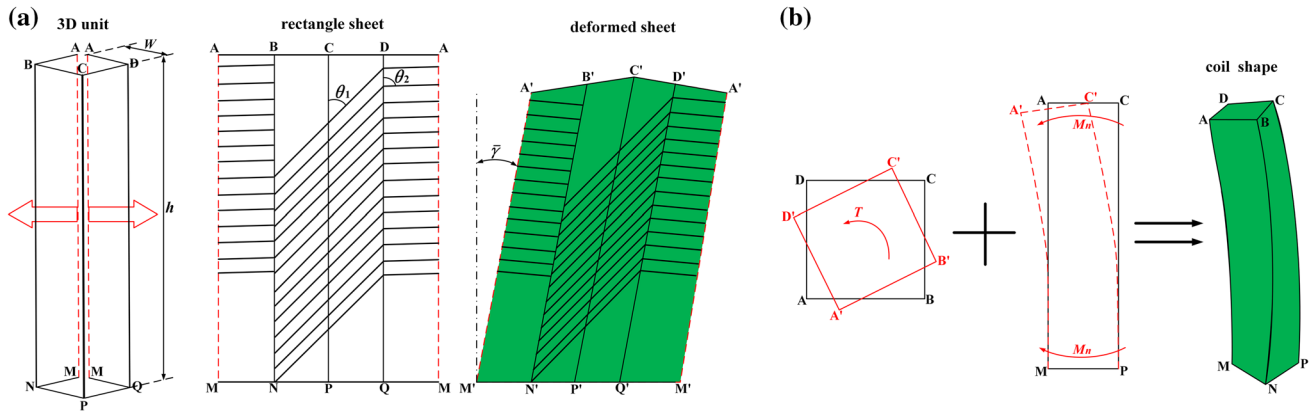

Fig. 8 Deformation of the cell wall model during shrinkage with tilted helix cellulose fibers. **a** A small cube extracted from the cell wall virtually cut open along a *vertical line* (AM) and deforms from the *rectangular sheet* into a pentagonal according to the shrinkage process; $\bar{\gamma}$: turn angle of the whole deformed sheet according to the assumption that the *bottom line* of the sheet remains in the same plane. **b** Schematic illustration of the coiling deformation of the cell wall model. The tilted helix arrangement of the stiff cellulose fibers can direct the shrinkage forces, so as to form a torque (T) and a bending movement (M_n), simultaneously.

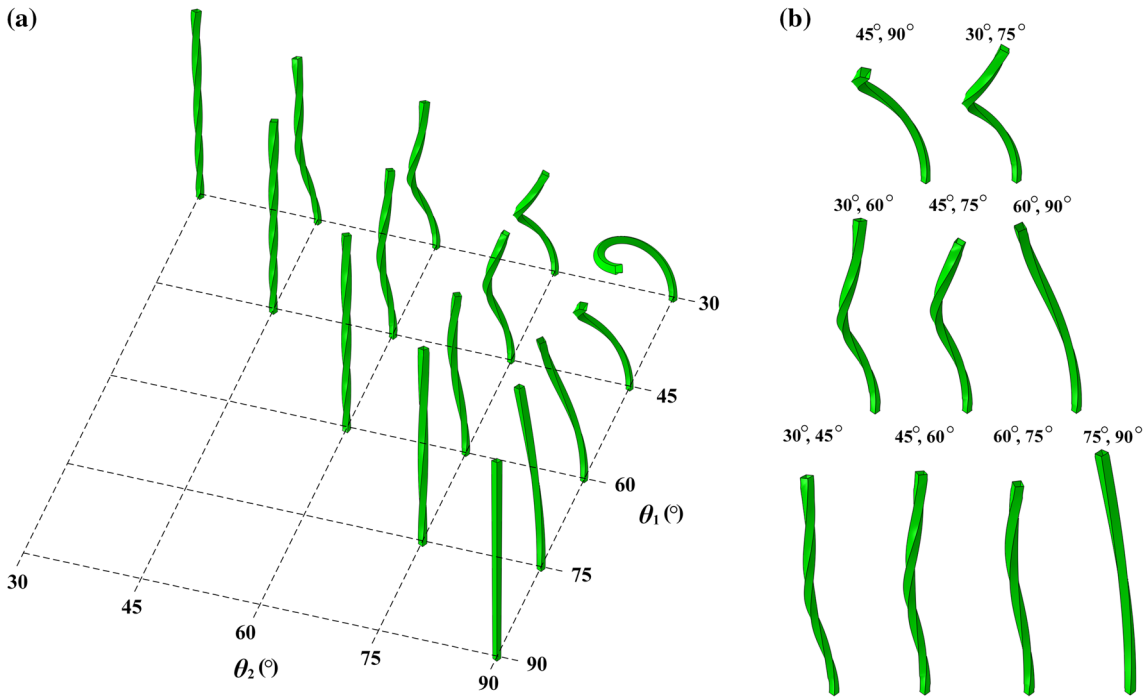

Fig. 9 **a** FE simulation results of tube models with different magnitudes of θ_1, θ_2 and θ_t. **b** Simulation results of three groups of tube models and θ_t of the models in each group are the same.

are the same, shape of the deformed tubes are quite different. Then two parameters are defined as: $\overline{\gamma} = \frac{(\gamma_1+\gamma_2)}{2}$ and $\Delta\varepsilon = |\varepsilon_{h2} - \varepsilon_{h1}|$. Combine the results shown in Fig. 9b and Table 3, a regularity could be found that: torsion and curvature of the curve are proportional to the magnitudes of $\overline{\gamma}$ and $\Delta\varepsilon$, respectively.

Simulation results of one finite element cell wall model

To further analyze the influence of other factors on the coiling deformation, a FE model with smaller height (H = 520 μm) is built. Von Mises stresses on two

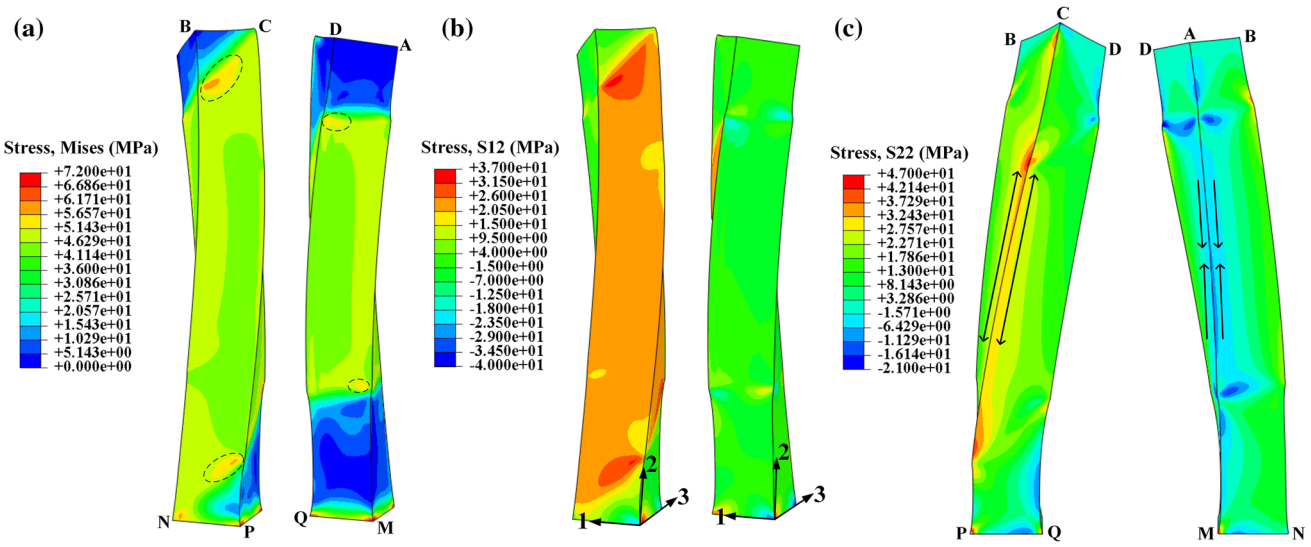

Fig. 10 **a** Von Mises stress distributions in two representative shells with different MFAs ($\theta_1 = 51°$, $\theta_2 = 89°$), regions of the stress concentration are surrounded by the *ellipses*, **b** Shear stress (S12) distributions in these two shells (*axes* represent the local coordinate systems), **c** Axial stress (S22) distributions in the shells opposite to each other (*arrows* indicate the directions of the axial stresses).

Table 1 Values of θ_1, θ_2 and θ_t in the FE models

Model number	θ_1 (°)	θ_2 (°)	θ_t (°)
1	30	30	0
2	45	45	0
3	60	60	0
4	75	75	0
5	30	45	7.5
6	30	60	15
7	30	75	22.5
8	30	90	30
9	45	60	7.5
10	45	75	15
11	45	90	22.5
12	60	75	7.5
13	60	90	15
14	75	90	7.5

Table 2 Structural parameters of each FE model

E_f (GPa)	E_m (GPa)	H (μm)	W (μm)	t (μm)	F	ΔV (%)
135	0.6	2580	70	4	0.5	24

representative shells are selected to illustrate stress distributions of the model. MFAs of the first (shell BNPC) and second shell (shell DQMA) are $\theta_1 = 51°$ and $\theta_2 = 89°$, respectively. As shown in Fig. 10a, due to the anisotropic architecture of the fiber skeleton, high Mises stresses exhibit in the regions closer to the ends of overall skeleton (surrounded by the ellipses). Under the effect of T, these two shells are subject to a pair of shear stresses with the same direction (Fig. 10b). Moreover, magnitude of the shear stresses distributed in the stress concentration regions are apparently higher than those distributed in other area. As shown in Fig. 10c, it can be found that under the effect of M_n, opposite sides of the FE model are subject to a pair of axial stresses with different directions (tensile and shrinkage). Then, the coiling deformation was characterized by the torsional angle (ϕ_t) of top surface of the model (ABCD) and its deflection ($\boldsymbol{y}$). Figure 11 shows these two parameters are both as linear functions of ΔV. In addition, the torsional angle per unit length ϕ_0 ($\phi_0 = \phi_t/H$) of the coil is 0.0762 (°/μm). This means that height of the tube model formed a complete turn of the coil is about 2362 μm ($H_t = 180°/\phi_0 = 2362\mu m$). According to the measurement of 20 fresh awn specimens, it is found that the length of active awns (without seed and tail) under saturated state are 14.8 ± 1.5 mm and the number of turns in the awns under completely dry state are 7 ± 1. Thus, length of the awn tissue composed of each turn is approximately 2114 μm. These results show that the FE models developed in this study capture the essential feature of the coiling behavior of the cells during moisture evaporation.

Configuration of the tilted helix fiber skeletons

Effect of the fiber configuration on the coiling deformation is investigated based on FE method. A series of FE models with different F are developed. In these models, the fiber profile radius $r = 1$, F of the fiber skeleton changed from 0.066 to 0.5, and other structural parameters remain unchanged. To better illustrate the stress distributions inside the fiber reinforced models, one scale bar is used for the fiber skeleton, another scale bar is used for the matrix shell. As shown in Fig. 12, when the magnitudes of F are high, stresses are uniformly distributed throughout the entire model, relatively. However, each reinforced fiber will take up more stresses with decreasing of F. To study this phenomenon further, two other groups of FE models with different fiber profile radius ($r_{0.5} = 0.5$ μm, $r_{1.5} = 1.5$ μm) are proposed for comparison. Then, values of ϕ_t and $\boldsymbol{y}$ of the deformed FE models belong to all three groups were plotted in Fig. 13a and b, respectively. The results indicate that change of F and r have certain effect on the coiling deformation. Based on these results, the configuration parameters of fiber skeleton at $F = 0.5$ and $r = 1$ are determined in the following sections.

Table 3 $\bar{\gamma}$ and $\Delta\varepsilon$ for models with different θ_1 and θ_2, as calculated from (4) and (5) under the condition of $\varepsilon_\theta = 0.16$

θ_1(°), θ_2(°)	45, 90	30, 75	30, 60	45, 75	60, 90	30, 45	45, 60	60, 75	75, 90
$\bar{\gamma}$ (°)	4.97	6.81	8.63	7.47	4.31	9.28	9.28	6.81	2.50
$\Delta\varepsilon$	0.069	0.10	0.079	0.061	0.032	0.042	0.037	0.024	0.0081

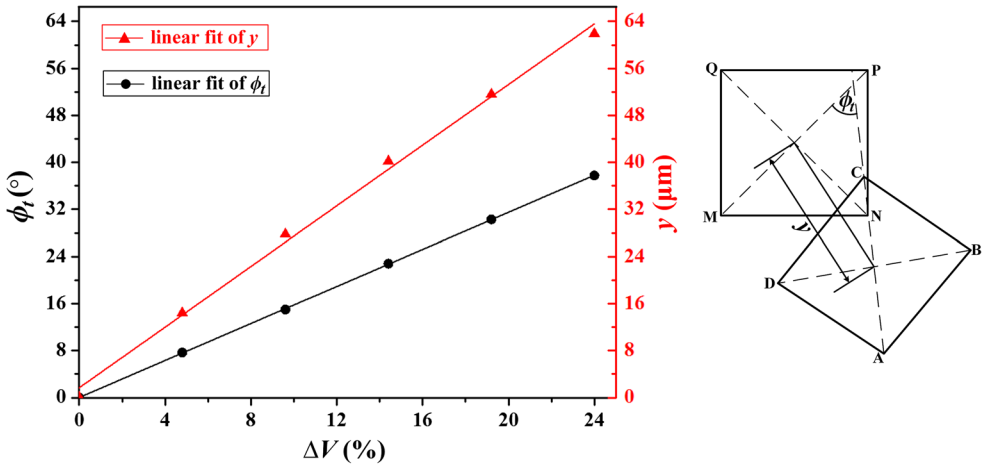

Fig. 11 FE simulation results of one fiber reinforce model indicate that: degree of the coiling deformation increasing substantially with the increase of ΔV and the line graph shows that the torsional angle ϕ_t and the deflection y of the coiling are both linear function of ΔV (definition of ϕ_t and y indicated by the schematic diagram at the right side of the line graph).

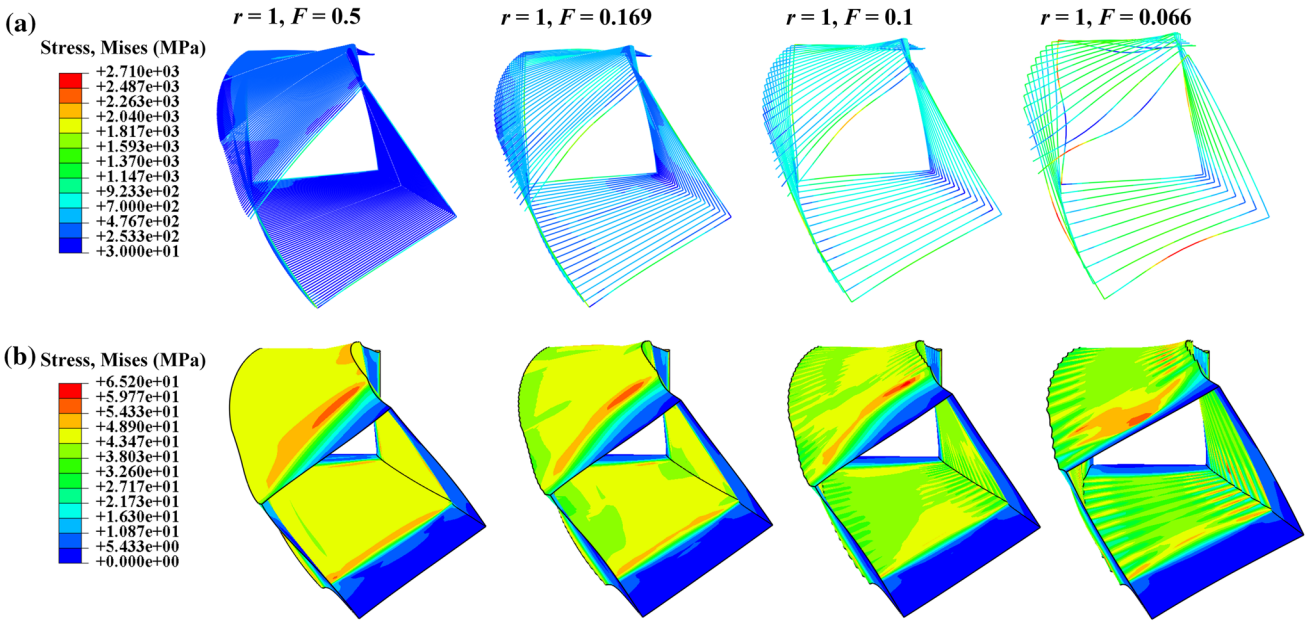

Fig. 12 Von Mises stress distributions in the FE models for different fiber frequency (F) ranging from 0.066 to 0.5. *Scale bar* **a** is for the fiber skeletons, and *scale bar* **b** is for the matrix shells.

Modulus ratios between fibers and matrix

The effect of modulus ratios (E_f:E_m) on the coiling deformation is studied and the fiber-matrix modulus ratios ranged from 1:1 to 160:1. Then, ϕ_t and y of the deformed FE models are plotted with respect to different modulus ratios (Fig. 14). The graph shows that both ϕ_t and y are increasing with the increase of E_f:E_m drastically, while their magnitudes do not change substantially when the ratio exceeding 40:1. Representative strain contours of the fiber skeleton with different modulus ratios of 120:1, 40:1, 15:1, 25:3, 5:1 and 5:3 were shown in Fig. 15. To better illustrate the shrinkage strain, scale bar of the contours are spectrums with reversed rainbow. When modulus ratio is low, the fiber skeleton generates considerable shrinkage strain in fiber direction (high magnitude of ε_f). In brief, in aspect of the coiling deformation, the most important mechanical property of the cell wall is the modulus ratio E_f:E_m.

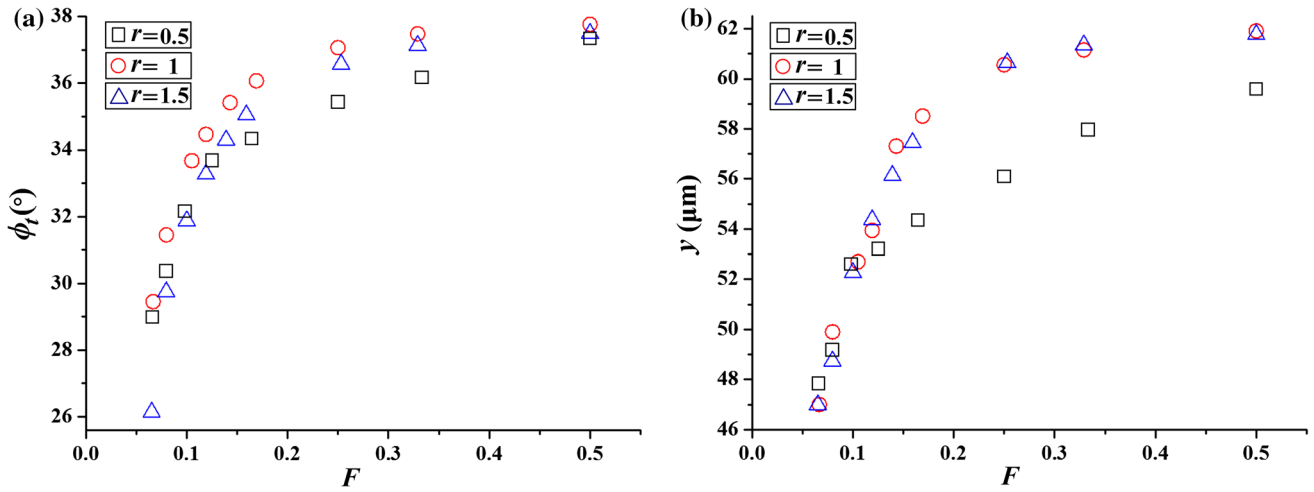

Fig. 13 Interdependency of fiber frequency (F), fiber profile radius (r), **a** torsional angles (ϕ_t), and **b** deflections (y), according to the coiling deformation of the FE models.

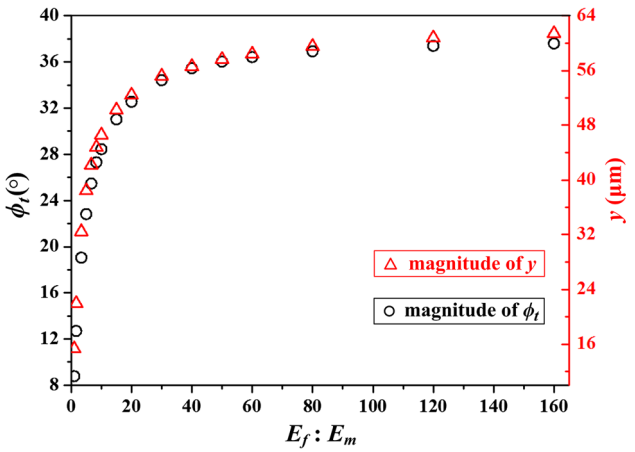

Fig. 14 Plots of the torsional angles (ϕ_t) and deflections (y) from the deformed FE models at different fiber-matrix modulus ratios (E_f:E_m) ranging from 1:1 to 160:1.

Macroscopical combination among the FE models

Based on the 3D morphology features of the inner layer of the awn tissue shown in Fig. 4d, an abnormal middle lamella region was observed between two end-to-end cells due to anisotropic structure of the fiber skeletons. We investigate the effect of this characteristic on the macroscopic deformation of the cells aligned with the longitudinal direction by a link chain model. The new model consists of 11 end-to-end FE models with different height (H_1 = 520 μm, H_2 = 380 μm). As shown in Fig. 16a, when overall length of the link chain (L) reaches 5020 μm, one column of deformed FE models come into being a complete cycle (two turns) of the coil. Then, the active part of the fresh awn is cut crosswise to divide it into several sections with different widths. Shape of the awn section with very narrow width is similar to the deformed FE link chain model (Fig. 16b). As shown in Fig. 16c, when L change from 520 to 5020 μm, ϕ_t of the coils increase linearly while magnitudes of their ϕ_0 stay almost the same.

Furthermore, deformation of two FE models connected side-to-side by a thin middle lamella is studied (Fig. 17a). In these new models, elastic modulus of the middle lamella (E_{md}) are considered as variables. Then, magnitudes of ϕ_t and y of the deformed models with respect to different E_{md} are plotted in Fig. 17b. The results show that when E_{md} keeps in the range of 1–100 MPa, magnitudes of ϕ_t will decrease with the increasing of E_{md}, while y increases accordingly. When the middle lamella is softer than 10 MPa, the constraint effect on torsion will become very weak but the magnitudes of y are still greater than that of single cell models. Finally, combined twenty FE models with different height together, the study constructed a new tissue model (E_{md} = 5 MPa). As shown in Fig. 17c, this part of tissue still generates a deformation with tendency of coiling.

Discussion

Abraham et al. first proposed that arrangement of the cellulose fibers within the coiling cell of *Geraniaceae* are the tilted helix with very small pitch [11–13]. However,

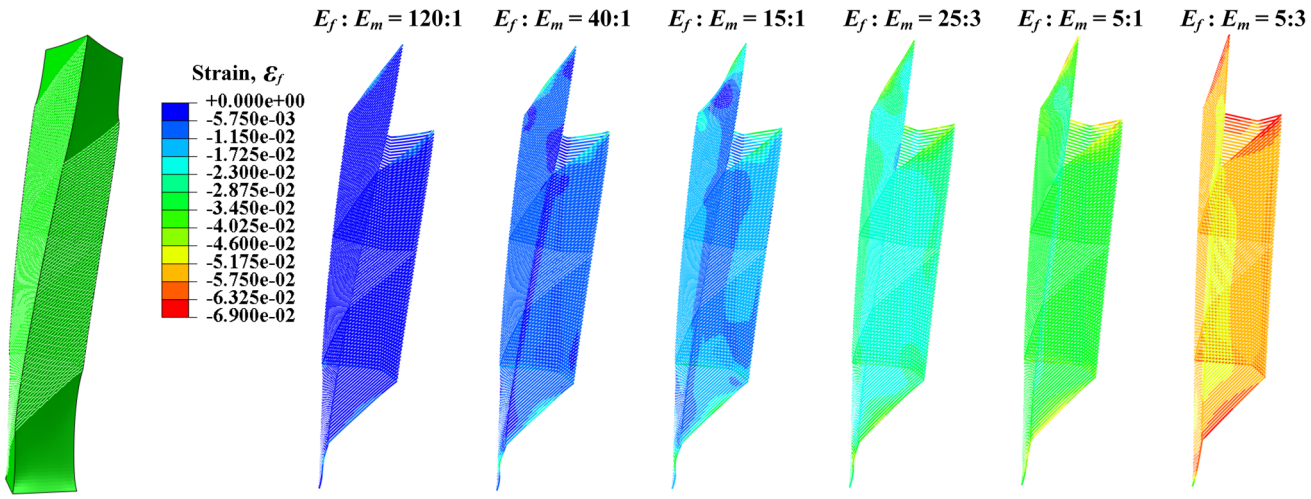

Fig. 15 Representative contours of strain in the fiber direction (ε_f) from the fiber skeleton in the case of fiber-matrix modulus ratios at 120:1, 40:1, 15:1, 25:3, 5:1 and 5:3, respectively.

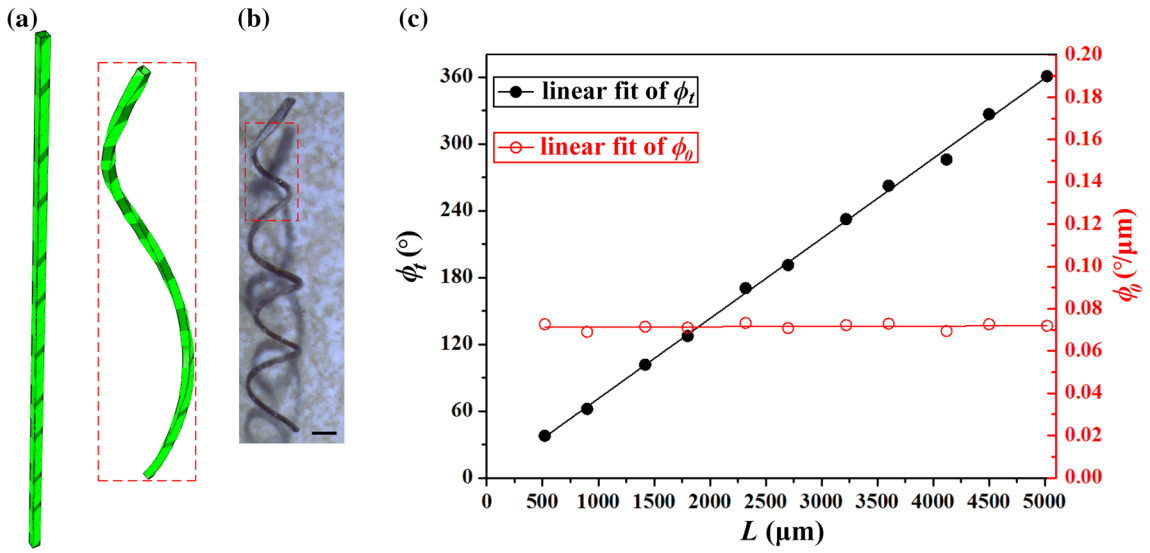

Fig. 16 **a** FE simulation result of eleven fiber reinforced models aligned with the longitudinal direction. **b** Morphology image of the coil awn section with the width of about 0.15 mm (*scale bar* 0.5 mm). **c** Plots of torsional angles (ϕ_t) and torsional angle per unit length (ϕ_0) from the deformed link chain models at different lengths ranging from 520 to 5020 μm.

huge stiffness of the continuous cellulose fibers will definitely restrain deformation of the cell. Combined the 3D morphology exported by the micro-CT (Fig. 5d) and 2D SAXS patterns, we proposed that numerous cellulose fibers aligned with the cell axis direction, constituted the complete fiber skeleton of the cell wall. Gaps between two adjacent fibers could make the strain occur in the direction that is normal to the fibers more easily. Most researchers in this field put emphasis on the measurement of the tilt angle (θ_t) and inferred that configuration of the coiling cell depend strongly on it. The mechanical studies in this paper illustrated that shape of the deformed cell model would convert from twist to coil gradually with increase of θ_t. But the mechanism is more complicated. In addition to θ_t, two other parameters $\overline{\gamma}$ and $\Delta\varepsilon$ defined in this paper could also influence the deformation significantly. The models proposed in "Simplified mechanical model of the inner layer cell wall" section are derived from the biomaterial. But it may be applicable to other composites with complicated deformation behavior.

A series of cell wall models had been proposed to study the anisotropic swelling or shrinkage behavior of plant

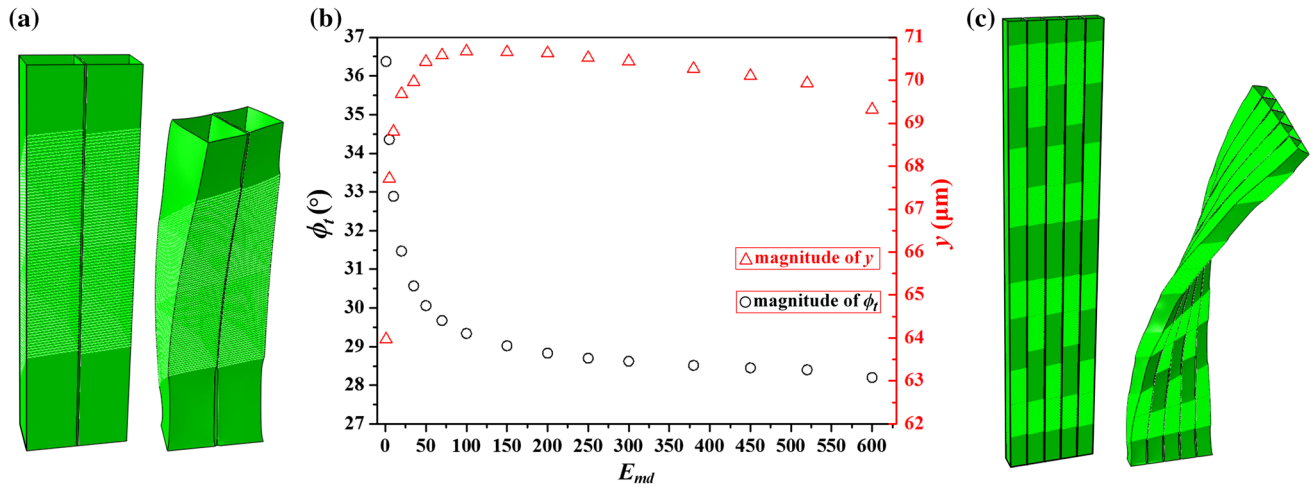

Fig. 17 **a** FE simulation result of two fiber reinforced models connected side-to-side by a thin middle lamella with elastic modulus of E_{md}. **b** Plots of the torsional angles (ϕ_t) and deflections (y) from the deformed FE models at different E_{md} ranging from 1 to 600 MPa. **c** FE simulation result of deformation of the tissue model consisted of 20 fiber reinforced models.

cells [38–42]. Equilibrium conditions of these mechanical models were mainly under the assumption that the cellulose fibers can be regarded as inextensible. In addition, the specific configuration of the fiber skeleton within the cell wall and mechanism of connection among the cells were not taken into account in these models. Based on the results shown in Fig. 12 and Fig. 13, it could be found that the configuration parameter F of the fiber skeleton will evidently influence the stress distribution pattern in the whole cell wall, and its deformation. When r was kept constant and the magnitudes of F were low, high Mises stresses will exist in the fibers-matrix interface (Fig. 12). Huge stiffness of the fibers will restrict the strain of matrix which were jointed (in the fiber direction), thus deformation of the whole model decrease macroscopically. Under the same F, and size of r meet the condition: ($\frac{2r}{t} > \frac{1}{2}$), continuously increasing r had relatively negligible influence on degree of the coiling deformation (Fig. 13). Even though it will increase the fiber volume fraction. According to the results shown in Fig. 14 and Fig. 15, boundary of the concept "inextensible" of the reinforced fibers was found. When the modulus ratio E_f:E_m was lower than 40:1, the hypothesis of "inextensible fiber" will not be tenable any more and the anisotropy of the shrinkage deformation decrease substantially. When applying the fiber skeleton with this kind of special tilted helix structure in biomimetic devices, it is suggested that the modulus ratios between the fiber and matrix of the composite should exceed 40:1.

According to the results shown in Fig. 16, it was found that even though the anisotropic structure of the fiber skeleton will make high Mises stresses exhibited in the connection part between two end-to-end cells. But this feature had relatively negligible influence on the coiling deformation of the cells aligned with the longitudinal direction. Both mechanically and chemically isolated wood fibers showed an anti-clockwise twist according to change in water content [42] [43]. However, in normal wood tissues, the heavily lignified middle lamella reducing the ability of cells to deform against each other in shearing thus their torsional deformation were restrained [40]. *P. peltatum* for contrast, the inner layer cells within its awn were bonded by a thin middle lamella. Structure of the middle lamella were relatively loose and had many small cavities (Fig. 5c). Combining these morphological characteristics and results of the FE analysis (Fig. 17b), it could be found that soft middle lamella may help the tissue generate more pronounced coiling deformation.

Conclusions

The coiling movements of awns in *P. peltatum* seed caused by anisotropic shrinkage behavior of its inner layer cell wall are controlled by the structure of stiff cellulose fiber skeleton embedded in the hygroscopic matrix:

(1) Fibers of the skeleton arranges in the tilted helix with two different MFAs. In contrast to a normal helix, difference between these two MFAs

(θ_t) could direct the deformed cell convert from twist to coil. Moreover, torsion and curvature of the coil are proportional to the parameters $\overline{\gamma}$ and $\Delta\varepsilon$, respectively.

(2) Degree of the coiling deformation increases substantially with the increase of volume strain. During the deformation process, high Mises stresses exhibited in the regions that is closer to two ends of one cell wall.

(3) High frequency of the fiber skeleton will increase uniformity of the stresses, and then, the degree of coiling.

(4) The anisotropic shrinkage of cell wall was based on the fact that cellulose fibers were infinitely stiff compared to the soft matrix. When developed a biomimetic fibrous actuator based on the inspiration from inner layer cell of the awn, it is strongly suggested that the modulus ratio between the fibers and matrix material should exceed 40:1.

(5) The lateral sides of two adjacent inner layer cells are bound by a thin middle lamella layer with pore structure. Finite element analysis results show that soft middle lamella may improve the coiling behavior of the tissue.

In conclusion, the biophysical principles revealed by the inner layer cell of the coiling awn tissue may help to develop a new kind of artificial penetrator with small size and light weight. This penetrator would not require additional energy source and electronic control system. The architecture of reinforcement fibers should be programmed in advance to attain passive actuation of the whole composite.

Compliance with ethical standards

Conflict of interest The authors declare that they have no conflict of interest.

References

[1] Burgert I, Fratzl P (2009) Actuation systems in plants as prototypes for bioinspired devices. Phil Trans R Soc A 367:1541–1557

[2] Dawson C, Vincent JFV, Rocca AM (1997) How pine cones open. Nature 390:668

[3] Reyssat E, Mahadevan L (2009) Hygromorphs: from pine cones to biomimetic bilayers. J R Soc Interface 6:951–957

[4] Ingold CT (1959) Peristome teeth and spore discharge in mosses. Trans Proc Bot Soc 38:76–88

[5] Hegazy AK, Barakat HN, Kabiel HF (2006) Anatomical significance of the hygrochastic movement in *Anastatica hierochuntica*. Ann Bot-London 97:47–55

[6] Armon S, Efrati E, Kupferman R, Sharon E (2011) Geometry and mechanics in the opening of chiral seed pods. Science 333:1726–1730

[7] Elbaum R, Zaltzman L, Burgert I, Fratzl P (2007) The role of wheat awns in the seed dispersal unit. Science 316:884–886

[8] Elbaum R, Gorb S, Fratzl P (2008) Structures in the cell wall that enable hygroscopic movement of wheat awns. J Struct Biol 164:101–107

[9] Stamp NE (1984) Self-burial behaviour of *Erodium cicutarium* seeds. J Ecol 72:611–620

[10] Evangelista D, Hotton S, Dumais J (2011) The mechanics of explosive dispersal and self-burial in the seeds of the filaree, *Erodium cicutarium* (*Geraniaceae*). J Exp Biol 214:521–529

[11] Abraham Y, Tamburu C, Klein E, Dunlop JWC, Fratzl P, Raviv U, Elbaum R (2012) Tilted cellulose arrangement as a novel mechanism for hygroscopic coiling in the stork's bill awn. J R Soc Interface 9:640–647

[12] Abraham Y, Elbaum R (2013) Hygroscopic movements in *Geraniaceae*: the structural variations that are responsible for coiling or bending. New Phytol 199:584–594

[13] Abraham Y, Elbaum R (2013) Quantification of microfibril angle in secondary cell walls at subcellular resolution by means of polarized light microscopy. New Phytol 197:1012–1019

[14] Wonjong J, Wonjung K, Ho-Young K (2014) Self-burial mechanics of hygroscopically responsive awns. Integr Comp Biol 54:1034–1042

[15] Tirrell DA (1994) Hierarchical structures in biology as a guide for new materials technology. National Academy Press, Washington DC

[16] Barnett JR, Bonham VA (2005) Cellulose microfibril angle in the cell wall of wood fibres. Biol Rev 79:461–472

[17] McNeil M, Darvill AG, Fry SC, Albersheim P (1984) Structure and function of the primary cell walls of plants. Ann Rev Biochem 53:625–663

[18] Carpita NC, Gibeaut DM (1993) Structural models of primary cell walls in flowering plants: consistency of molecular structure with the physical properties of the walls during growth. Plant J 3:1–30

[19] Reiter WD (1998) The molecular analysis of cell wall components. Trends Plant Sci 3:27–32

[20] Kerstens S, Decraemer WF, Verbelen JP (2001) Cell walls at the plant surface behave mechanically like fiber-reinforced composite materials. Plant Physiol 127:381–385

[21] Fratzl P, Burgert I, Keckes J (2004) Mechanical model for the deformation of the wood cell wall. Z Metallkd 95:579–584

[22] Burgert I, Fratzl P (2009) Plants control the properties and actuation of their organs through the orientation of cellulose fibrils in their cell walls. Integr Comp Biol 49:69–79

[23] Baskin TI (2005) Anisotropic expansion of the plant cell wall. Annu Rev Cell Dev Bl 21:203–222

[24] Fahn A, Werker E (1972) Seed biology. In: Kozlowski TT (ed) Anatomical mechanisms of seed dispersal. Academic Press, New York, pp 152–221

[25] Lacey EP, Kaufman PB, Dayanandan P (1983) The anatomical basis for hygroscopic movement in primary rays of *Daucus carota* ssp. *carota* (*Apiaceae*). Bot Gaz 144:371–375

[26] Forterre Y, Dumais J (2011) Generating helices in nature. Science 333:1715–1716

[27] Jungnikl K, Goebbels J, Burgert I, Fratzl P (2009) The role of material properties for the mechanical adaptation at branch junctions. Trees 23:605–610

[28] Slater D, Bradley RS, Withers PJ, Ennos AR (2014) The anatomy and grain pattern in forks of hazel (*Corylus avellana* L.) and other tree species. Trees 28:1437–1448

[29] Kroon-Batenburg LMJ, Kroon J, Norholt MG (1986) Chain modulus and intramolecular hydrogen bonding in native and regenerated cellulose fibers. Polym Commun 27:290–292

[30] Nishino T, Takano K, Nakamae K (1995) Elastic modulus of the crystalline regions of cellulose polymorphs. J Pol Sci Pol Phys 33:1647–1651

[31] Saavedra Floresa EI, de Souza Netob EA, Pearcec C (2011) A large strain computational multi-scale model for the dissipative behavior of wood cell-wall. Comp Mater Sci 50:1202–1211

[32] Hepworth DG, Bruce DM (2000) A method of calculating the mechanical properties of nanoscopic plant cell wall components from tissue properties. J Mater Sci 35:5861–5865

[33] Cousins WJ (1976) Elastic modulus of lignin as related to moisture content. Wood Sci Technol 10:9–17

[34] Cousins WJ (1978) Young's modulus of hemicellulose as related to moisture content. Wood Sci Technol 12:161–167

[35] Salmén L (2001) Proceedings of 1st International Conference of the European Society for Wood Mechanics. In: Navi P (ed) Micromechanics of the wood cell wall: a tool for the better understanding of its structure. EPFL, Lausanne, pp 385–398

[36] Salmén L (2004) Micromechanical understanding of cell-wall structure. C R Biol 327:873–880

[37] Zamil MS, Yi H, Virendra MP (2015) The mechanical properties of plant cell walls soft material at the subcellular scale: the implications of water and of the intercellular boundaries. J Mater Sci 50:6608–6623

[38] Spatz HC, Köhler L, Niklas KJ (1999) Mechanical behaviour of plant tissues: composite materials or structures? J Exp Biol 202:3269–3272

[39] Yamamoto H, Sassus F, Ninomiya M, Gril J (2001) A model of anisotropic swelling and shrinking process of wood. Wood Sci Technol 35:167–181

[40] Burgert I, Eder M, Gierlinger N, Fratzl P (2007) Tensile and compressive stresses in tracheids are induced by swelling based on geometrical constraints of the wood cell. Planta 226:981–987

[41] Neagu RC, Gamstedt EK (2007) Modeling of effects of ultrastructural morphology on the hygroelastic properties of wood fibers. J Mater Sci 42:10254–10274

[42] Burgert I, Frühmann K, Keckes J, Fratzl P, Stanzl-Tschegg S (2005) Properties of chemically and mechanically isolated fibres of spruce (*Picea abies* [L.] Karst.). Part 2: twisting phenomena. Holzforschung 59:247–251

[43] Meylan BA, Butterfield BG (1978) Helical orientation of the microfibrils in tracheids, fibres and vessels. Wood Sci Technol 12:219–222